An altimetry-based gravest empirical mode south of Africa:
1. Development and validation

Sebastiaan Swart,[1] Sabrina Speich,[2] Isabelle J. Ansorge,[1] and Johann R. E. Lutjeharms[1]

[1] Hydrographic transects of the Antarctic Circumpolar Current (ACC) south of Africa are projected into baroclinic stream function space parameterized by pressure and dynamic height. This produces a two-dimensional gravest empirical mode (GEM) that captures more than 97% of the total density and temperature variance in the ACC domain. Weekly maps of absolute dynamic topography data, derived from satellite altimetry, are combined with the GEM to obtain a 16 year time series of temperature and salinity fields. The time series of thermohaline fields are compared with independent in situ observations. The residuals decrease sharply below the thermocline and through the entire water column the mean root-mean-square (RMS) error is 0.15°C, 0.02, and 0.02 kg m^{-3} for temperature, salinity, and density, respectively. The positions of ACC fronts are followed in time using satellite altimetry data. These locations correspond to both the observed and GEM-based positions. The available temperature and salinity information allow one to calculate the baroclinic zonal velocity field between the surface and 2500 dbar. This is compared with velocity measurements from repeat hydrographic transects at the GoodHope line. The net accumulated transports of the ACC, derived from these different methods are within 1–3 Sv of each other. Similarly, GEM-produced cross-sectional velocities at 300 dbar compare closely to the observed data, with the RMS difference not exceeding 0.03 m s^{-1}. The continuous time series of thermohaline fields, described here, are further exploited to understand the dynamic nature of the ACC fronts in the region, and which is given by Swart and Speich (2010).

Citation: Swart, S., S. Speich, I. J. Ansorge, and J. R. E. Lutjeharms (2010), An altimetry-based gravest empirical mode south of Africa: 1. Development and validation, *J. Geophys. Res.*, *115*, C03002, doi:10.1029/2009JC005299.

1. Introduction

[2] The Antarctic Circumpolar Current (ACC) connects all three major ocean basins of the world and the exchanges that take place provide a vital mechanism for the Global Meridional Overturning Circulation. To date, observational studies in the Southern Ocean have relied largely on individual hydrographic transects that are often beset by low horizontal spatial resolutions caused by logistical constraints and harsh working conditions. Additionally, the Argo float program, while improving the observational coverage in recent years, still has a course spatial resolution and the data are only available from approximately 2003 (and 2004 for the region south of Africa). This proves problematic where basin-scale analysis is needed to recover transports and fluxes in the Southern Ocean. We attempt to address this problem in this study. Remotely sensed variables, such as altimetry, have in our opinion, been underutilized in providing information of the subsurface structure in the

Southern Ocean, and notably the ACC. Weekly maps of sea surface height (SSH) data from 1992, sampled at a relatively high spatial resolution, provide us with a base with which to investigate the dynamic variability and structure of the ACC system.

[3] Localised strong meridional gradients in thermohaline properties (otherwise known as baroclinic fronts) are an ubiquitous feature of the Antarctic Circumpolar Current. An Eulerian approach to monitoring these fronts reveals high levels of temporal variability associated with their recurrent meandering and shifting, caused by mesoscale eddy shedding, as well as seasonal to interannual variations. To overcome this problem, hydrographic sections should be aligned with a common origin, such as the position of a baroclinic front determined using specified criteria.

[4] We can project hydrographic sections onto a baroclinic stream function coordinate $\Gamma(p, \phi)$ (in this case dynamic height at the sea surface, referenced to a common pressure, ϕ_{2500}) in order to give us insight into the subsurface thermohaline structure of the ACC. Thus, this method allows one to obtain the thermohaline properties of the water column from any particular measurement of dynamic height. This projection is called the gravest empirical mode (GEM) and was first introduced to Southern Ocean hydrography through a series of studies by *Sun and Watts* [2001, 2002] and *Watts et al.* [2001]. The GEM is specifically

[1] Department of Oceanography, University of Cape Town, Rondebosch, South Africa.
[2] Laboratoire de Physique des Océans, UMR 6523, Université de Bretagne Occidentale, CNRS, IFREMER, Brest, France.
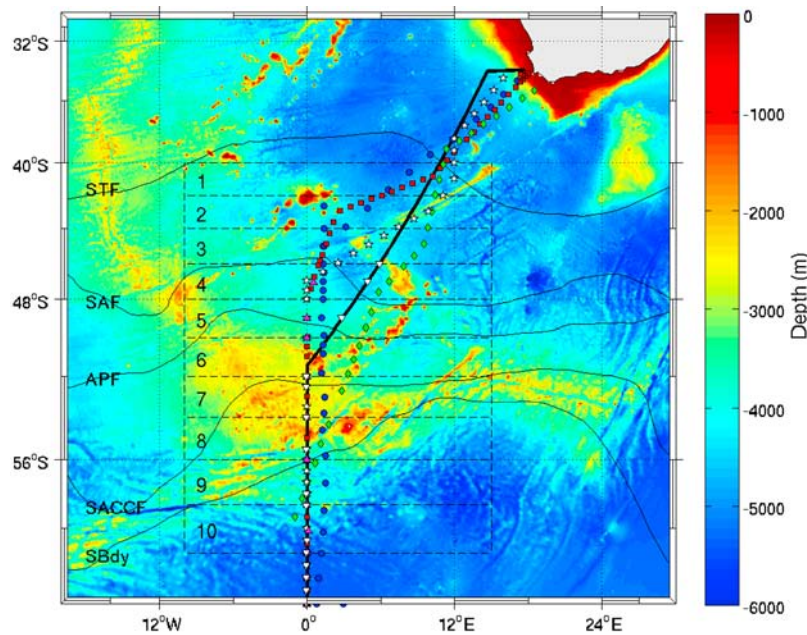
Figure 1. Locations of the eight CTD sections used in this study. The AJAX section (blue circles), A21 section (green diamonds), 1992 A12 section (red squares), 1999 A12 section (magenta triangles), 2000 A12 sections (white stars), and 2002 A12 section (white triangles). The solid black line represents the repeat cruise track of the GH CTD and XBT sections. Traces of the ACC fronts, by *Orsi et al.* [1995], and the bathymetry (in m) has been overlaid. STF, Subtropical Front; SAF, Subantarctic Front; APF, Antarctic Polar Front; SACCF, southern ACC front; SBdy, southern boundary of the ACC. The gridded boxes represent the latitudinal zones from which Argo float data were extracted to derive a seasonal model for the region.

advantageous for removing a large fraction of the temporal variability associated with small-scale and transient features. This is appealing for general circulation studies as only the modal field is represented. The GEM projected field is also time invariant, vertically coherent, and equivalent barotropic [*Sun and Watts*, 2001].

[5] The focus of this study lies in the ocean region south of Africa. The GoodHope (GH) monitoring program [*Ansorge et al.*, 2004; *Speich and Arhan*, 2007; *Swart et al.*, 2008; *Gladyshev et al.*, 2008] (Figure 1) provides the ideal platform to combine the GEM with satellite altimetry SSH data and demonstrate the ability of this method to recreate in situ observations. This method provides us with a valuable 16 year time series (weekly intervals) of temperature and salinity fields at the GH line, which can be used to improve our understanding of the ocean dynamics in this least understood "choke point" of the ACC. Previous studies have already provided evidence that show that subsurface ocean information (such as upper ocean temperature and baroclinic transports) is closely correlated with the SSH signal [*Rintoul et al.*, 1997, 2002; *Sokolov et al.*, 2004; *Legeais et al.*, 2005; *Swart et al.*, 2008]. This emphasizes that SSH is representative of the density signal of the water column and that further information of the subsurface structure may be available by utilising knowledge of the SSH.

2. A Synopsis of the Hydrography at the GH Line

[6] Compared with Drake Passage and the oceanic region south of Australia, the African choke point constitutes the most variable of the Southern Ocean. South of Africa, three oceanic regimes dominate the hydrography: the Agulhas Current, the ACC, and the Weddell Gyre. The Agulhas Current, which lies along the south-eastern edge of the African continental shelf, is regarded the strongest western boundary current in the Southern Hemisphere. Its westward termination is marked by a region of extreme mesoscale variability [*Lutjeharms*, 2006] in the form of eddy shedding that is associated with the current retroflecting back toward the east [*Gordon*, 1985; *Duncombe-Rae*, 1991; *Lutjeharms*, 1996; *de Ruijter et al.*, 1999; *Boebel et al.*, 2003]. The Agulhas Retroflection produces an intermittent stream of Agulhas Rings [*Lutjeharms and Gordon*, 1987; *de Ruijter et al.*, 1999], which are occluded from the Agulhas Retroflection, and propagate generally in a north-westward direction [*Schouten et al.*, 2000], and intersect the GH line in the subtropical domain [*Gladyshev et al.*, 2008; *Swart et al.*, 2008]. On occasions an Agulhas Ring detaches from the Agulhas Retroflection and propagates in a west to south–west direction (a time series of altimetry data shows this to happen on average 2.7 occasions per year [see *Swart and Speich*, 2010; G. Dencausse et al., Routes of Agulhas rings in the southeastern Cape Basin, submitted to *Deep Sea Res. Part I*, 2009]). These features have been observed crossing the GH track between 39 and 42°S and are often observed well into the Subantarctic Zone (SAZ) [*Swart et al.*, 2008; *Gladyshev et al.*, 2008].

[7] The ACC is characterized by a series of eastward jets associated with baroclinic fronts, which denote the positions of the maximum meridional thermohaline gradients [*Deacon*, 1937; *Nowlin and Clifford*, 1982; *Orsi et al.*, 1995;
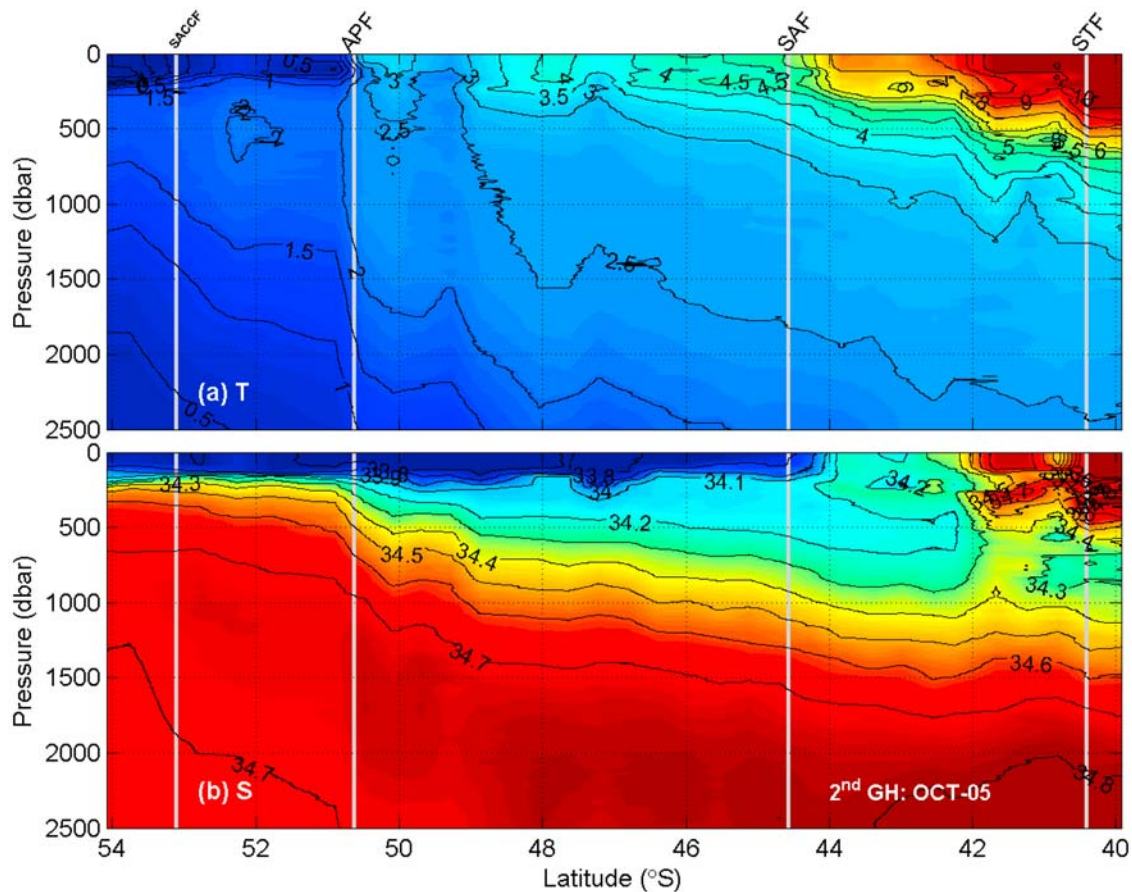
Figure 2. (a) Temperature and (b) salinity section from the second GH CTD section completed in October 2005. The ACC front locations, as determined using the criteria of *Orsi et al.* [1995], are indicated by the vertical grey lines.

Belkin and Gordon, 1996]. In the African sector of the Southern Ocean, four primary fronts exist: the Subtropical Front (STF), the Subantarctic Front (SAF), the Antarctic Polar Front (APF), and the southern ACC front (SACCF). Additionally, the southern boundary of the ACC (SBdy) marks the boundary separating flow between the ACC and Weddell Gyre system [*Orsi et al.*, 1993]. The presence and spatial structure of the STF south of Africa is complicated by the presence of Agulhas Rings, particularly in the region of the GH line. At this location, the presence of the STF is made up by an almost continual ''stream'' of eddies [*Lutjeharms*, 1988; *Lutjeharms and Valentine*, 1988; *Belkin and Gordon*, 1996; Dencausse et al., submitted manuscript, 2009].

[8] The hydrographic structure and frontal systems between Africa and Antarctica have been relatively well studied and described. Sea surface temperatures [e.g., *Lutjeharms and Valentine*, 1984], numerous expendable bathythermograph (XBT) sections [e.g., *Lutjeharms and Emery*, 1983; *Lutjeharms*, 1985; *Swart et al.*, 2008], some densely spaced conductivity-temperature-depth (CTD) sections [e.g., *Whitworth and Nowlin*, 1987; *Read and Pollard*, 1993; *Belkin and Gordon*, 1996; *Swart et al.*, 2008; *Gladyshev et al.*, 2008] and satellite observations [e.g., *Moore et al.*, 1999] have been used to describe the average geographic locations, average hydrographic characteristics and variations to all of these in substantial detail.

[9] The thermohaline structure, along the GH transect, is represented here by the second CTD occupation, completed in October 2005 (Figure 2). Each ACC temperature front, as defined by *Orsi et al.* [1995], is indicated on Figure 2. The CTD transect, unfortunately, did not cross the SBdy of the ACC so we are unable to represent it here. However, we choose to include this section because it is one of two sections in the region that is sampled at a high spatial resolution. This is important for clearly identifying more fine-scale features that can be missed by low spatial resolution CTD sections. The temperature and salinity sections clearly identify the principal water masses spanning the length of the section. The most obvious of these include warmer, saltier intrusions of Agulhas Water (consisting of Tropical Indian Surface Water and Subtropical Indian Surface Water) found north of ~40°S, Antarctic Intermediate Water (AAIW) characterized by a salinity minimum (34.4) layer extending north of ~50°S, and the temperature minimum layer at ~100 dbar located south of the APF placed at ~50.5°S.

3. Data

3.1. Conductivity-Temperature-Depth Data

[10] Data from eight CTD sections, completed between 1984 and 2005 (Table 1), are used to set up the GEM projection south of Africa. Most of the sections encompass

Table 1. Summary of the CTD Sections Used in This Study

Section	Date	Chief Scientist/Reference
AJAX	Jan 1984	T. Whitworth/*Scripps Institution of Oceanography* [1985]
A21	Jan–Mar 1990	W. Roether/*Roether et al.* [1990]
A12 1992	May–Aug 1992	P. Lemke/*Lemke* [1992]
A12 2000	Dec 2000	E. Fahrbach/*World Ocean Circulation Experiment* [2002]
A12 2002	Dec 2002	E. Fahrbach/*World Ocean Circulation Experiment* [2002]
GH1	Nov 2004	S. Gladyshev/*Gladyshev et al.* [2008]
GH2	Oct 2005	S. Gladyshev

the region between the south-western tip of South Africa and the Antarctic continent (see Figure 1), while some of the sections do not extend completely to Antarctica. The sections provide a relatively good coverage of the seasonal variability expected for the region. The two most recent sections were completed at the GH line and have a higher spatial resolution (∼50 km) than those completed earlier (∼80 km). In most cases, there was tighter station spacing over regions of shallow or steep bottom topography. In total, data from 296 CTD casts (of which 199 stations lie within the ACC domain) were used in this study. Data for the A12 sections, completed between 1999 and 2002, were obtained from the CLIVAR and Carbon Hydrographic Data Office (details pertaining to the sections can be found at http://whpo.ucsd.edu/). For further details regarding station spacing, CTD calibration and problems encountered refer to the following technical reports and papers by *Scripps Institution of Oceanography* [1985], *Roether et al.* [1990], *Lemke* [1992], *World Ocean Circulation Experiment* [2002], *Swart et al.* [2008], and *Gladyshev et al.* [2008].

3.2. Satellite Altimetry Data

3.2.1. Sea Level Anomaly

[11] The "Maps of Sea Level Anomaly (MSLA)" product from CLS/AVISO, a weekly SSH anomaly map on a $1/3°$ Mercator grid that incorporates data from T/P, Jason-1, ERS-1/2 and Envisat altimeters, was used in this study. This data set extends, at weekly intervals, from 14 October 1992 to 23 January 2008, yielding 798 weeks of data. Because the ACC is characterized by mesoscale structures and variability we choose to use the "up-to-date" data processing that makes use of all the satellite data available for each period. The satellite altimetry data, for this time series, are not homogeneous in number per unit time, but for long periods they provide an improved resolution and data accuracy compared with the classical "referenced" data set. These multimission gridded SSHs are referenced to a 7 year (1993–1999) mean. For details on mapping methods and error corrections applied to these fields, refer to *Le Traon et al.* [1998], *Le Traon and Ogor* [1998], and *Ducet et al.* [2000].

3.2.2. Absolute Dynamic Topography

[12] The Maps of Absolute Dynamic Topography (MADT) product from CLS/AVISO has the same temporal and spatial resolution as the data set described in section 3.2.1. The MADT is the sum of the sea level anomaly data and a mean dynamic topography (Rio05-Combined Mean Dynamic Topography (CMDT) [*Rio and Hernandez*, 2004]). The CMDT is a combined product using in situ measurements (hydrographic and surface drifter data), altimetry data and the EIGEN-GRACE 03S geoid. The CMDT is computed over a 7 year period (1993–1999).

We also make use of the absolute geostrophic velocities calculated from the MADT data that are available from CLS/AVISO.

3.3. Argo Float Data

[13] Argo profiling float data, from a quadrant located around the GH line and within the ACC (Figure 1), was used to set up a seasonal model for the region. The data comes from the Coriolis Operational Oceanography Center, which is one of two Argo Global Data Assembly Centres (GDAC) worldwide. Extensive quality control has been performed on the data, under the auspices of the GH observing program (M. Arhan and A. Prigent, personal communication, 2009). A total of 7120 individual profiles of temperature and salinity were located within this quadrant between January 2004 and October 2007. The profiles were then interpolated onto a regular pressure grid and placed within $2°$ latitudinal bands between the northern and southern ACC limits.

3.4. Expendable Bathythermograph Data

[14] The XBT data originates from six high-density sections completed at the GH line between February 2004 and March 2008. The XBTs were deployed to measure the upper ocean thermal structure at spatial intervals of 25 km, increasing the frequency to 15 km over the frontal regions of the ACC. The 4000 km transect between Africa and Antarctica was on average completed within 2 weeks, with each section providing a roughly synoptic picture of the upper thermal layer in this sector of the Southern Ocean.

[15] Extensive quality control procedures have been applied to the XBT data by AOML/NOAA in the United States. Adjacent temperature profiles were compared with each other and to the regional Levitus climatology [*Levitus*, 1982]. For more details on the AOML quality control procedures, refer to *Daneshzadeh et al.* [1994] and *Bailey et al.* [1994], and for more information on the XBT sections, refer to *Swart et al.* [2008].

4. Gravest Empirical Mode South of Africa

4.1. Projection in Stream Function Space

[16] The GEM is created by projecting the hydrographic data from eight CTD transects for the region, onto streamline coordinates of pressure and dynamic height (Figures 3a–3c and 4a–4c). Figures 3a–3c and 4a–4c illustrate the robust empirical relationship between the surface dynamic height and the vertical structure of temperature and salinity and the tendency for CTD data to cluster around a functional curve. We use 2500 dbar as the reference level because it is the deepest point that lies above the Mid-Ocean Ridge and also allows us to exploit CTD data that were not sampled to the
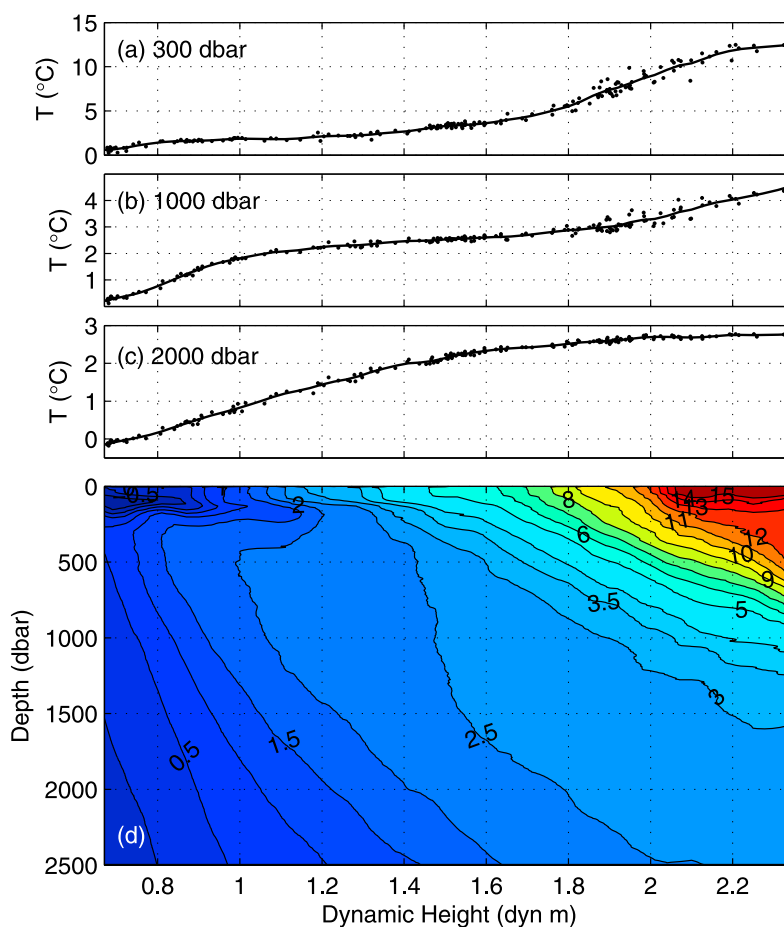
Figure 3. The available CTD temperature data plotted at three pressures, (a) 300, (b) 1000, and (c) 2000 dbar, as a function of dynamic height. A smoothing spline has been fitted to the data (solid curve). (d) The same data are used to create the GEM temperature field.

bottom due to time constraints and harsh weather conditions experienced during several of the cruises.

[17] In order to obtain a two-dimensional field using this projection method, we apply a cubic smoothing spline of equal parameter (Figures 3a–3c and 4a–4c) to each of the relationships between temperature/salinity and dynamic height, extending from the surface to 2500 dbar, at intervals of 5 dbar. The resulting two-dimensional fields for temperature and salinity are represented in Figures 3d and 4d, and are called GEM fields. Note that because these fields are represented using dynamic height, no explicit spatial information can be drawn from these sections. Although the GEM fields tend to suppress the fine-scale features associated with the ACC, the basic thermohaline structures are still present. The most distinct reproduced features are the subsurface temperature minimum layer located in the upper 200 dbar (Figure 3d), the surface salinity minimum layer, and the low saline waters associated with AAIW, which extend between the surface and ~1000 dbar (Figure 4d).

[18] In comparison to previous GEM constructions south of Australia (SR3 section [*Sun and Watts*, 2001]), the stream-function relationships are very similar (Figures 3a–3c and 4a–4c). In this study region, there is a greater scatter of temperature at the 1000 dbar interval, for values greater than the 2 dynamic (dyn) m (1 dyn m = 10 m^2 s^{-2}) interval

(Figure 3b). Similarly, the salinity structure experiences the same scattering, but at all shown pressure levels. This is primarily due to the close proximity of subtropical water masses bordering the northern limit of the ACC south of Africa, which introduce warmer, saltier waters through mesoscale variability at the STF and intruding Agulhas Rings [*Swart et al.*, 2008; *Swart and Speich*, 2010]. Besides the higher temperature and salinity signatures at dynamic heights greater than 1.8 dyn m, the respective GEM fields in Figures 3d and 4d are comparable to those south of Australia [*Sun and Watts*, 2001], while their GEM representations at 0°E are very similar to our GEM fields, although somewhat smoother likely due to different sampling resolutions and smoothing parameters used.

4.2. A Seasonal Model South of Africa

[19] Higher root-mean-square (RMS) residuals are associated with the upper mixed layer and are mainly caused by the seasonal cycle in both temperature and salinity. The CTD data have a seasonal bias because sampling generally takes place in spring-summer in the Southern Ocean, with the exception of the A12 1992 section. We therefore, rely on float data from the region to build a seasonal model in temperature and salinity, in the upper 500 dbar, to reduce this bias.
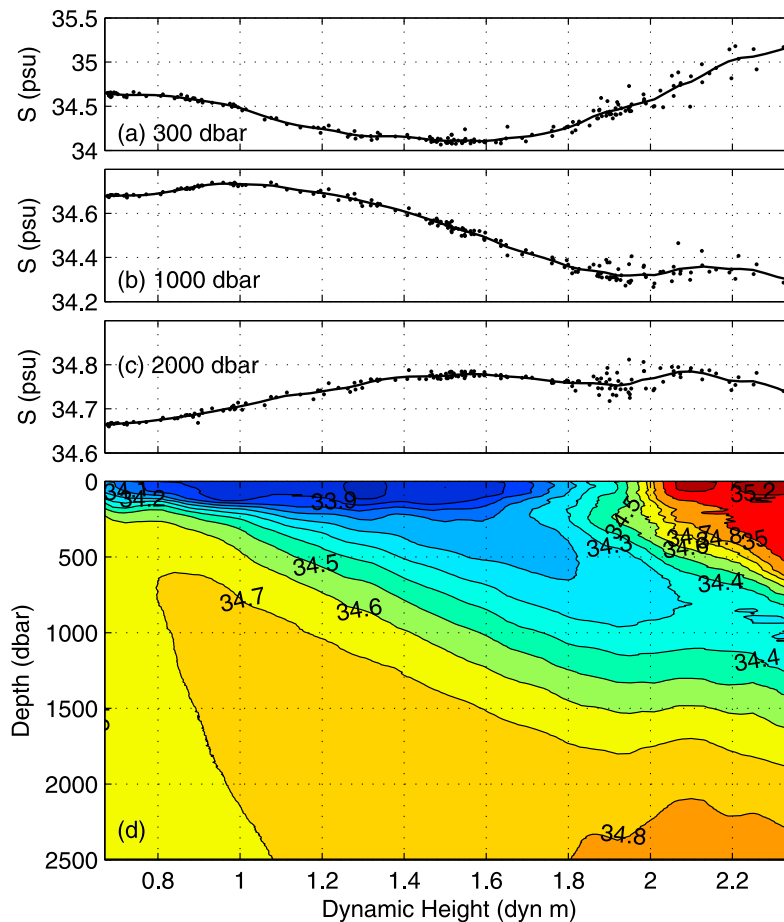
Figure 4. The same as Figure 3 but for salinity.

[20] Argo float profiles, gathered between 2004 and 2007, were grouped into 2° latitudinal bands between 40 and 60°S (Figure 1). This was done in order to preserve the changing seasonal model with change in latitude, while still acquiring enough profiles to create a sound seasonal pattern in that band. The data, averaged monthly, were replicated three successive times before a 3 month running mean was applied to the data to remove the intraseasonal variability. The middle year was extracted from the data set to avoid start and end transients during the filtering process. This mean cycle was then removed from the CTD data before being used to produce the GEM relationships. Therefore, all GEM data presented in this study have been parametrized by the seasonal model presented here. *Watts et al.* [2001] first employed this method for acoustic travel time, temperature and salinity data south of Australia.

[21] The seasonal cycle of temperature, combined for all latitudinal bands, (Figures 5a and 5b) shows a clear sinusoidal signal due to the surface warming (cooling) during austral summer (winter). At the surface, the transition from a warm to cool state takes place around mid-May while the reverse effect occurs during late November. A lag in this transition (∼5 months at 300 dbar) increases with pressure due to the delay in mixing to the deeper levels with time. The extent of the cool state, extends deeper than the summer warm state. This is likely due to stronger mixing and convective mechanisms taking place in the winter months,

which allows for cooling to take place beyond 300 dbar. The magnitude of the summer warming in the upper 100 dbar is, on average, ∼0.2°C higher than the winter cooling.

[22] The latitudinal differences in the annual cycle of salinity are more complicated than the temperature cycle. In order to avoid confusion, we only illustrate the annual salinity cycle between 56 and 58°S (Figure 5c). The general structure of the salinity cycle is similar to the temperature cycle except that the salinity cycle supersedes the temperature cycle by approximately 2 months. The deep extent of the salinity anomalies is likely caused by the extensive mixing of the upper ocean layers at the high latitudes where wind speeds are especially high.

[23] After applying the seasonal correction, the temperature RMS residual in the surface layer (0–300 dbar) is reduced from 0.22°C to 0.12°C. The salinity seasonal cycle has alternating positive and negative effects on reducing the RMS residual in the upper layers. In the upper 200 dbar, the seasonal correction causes the RMS residual to increase from 0.057 to 0.06, meanwhile, between the 200–300 dbar, the RMS residual decreases from 0.05 to 0.04. On average, applying the salinity seasonal correction reduces the RMS residuals in the upper layers and so it is used in this study even if its benefits are small.

4.3. Comparison Against Direct Measurements

[24] The GEM-derived temperature and salinity profiles were computed from the dynamic height, calculated from
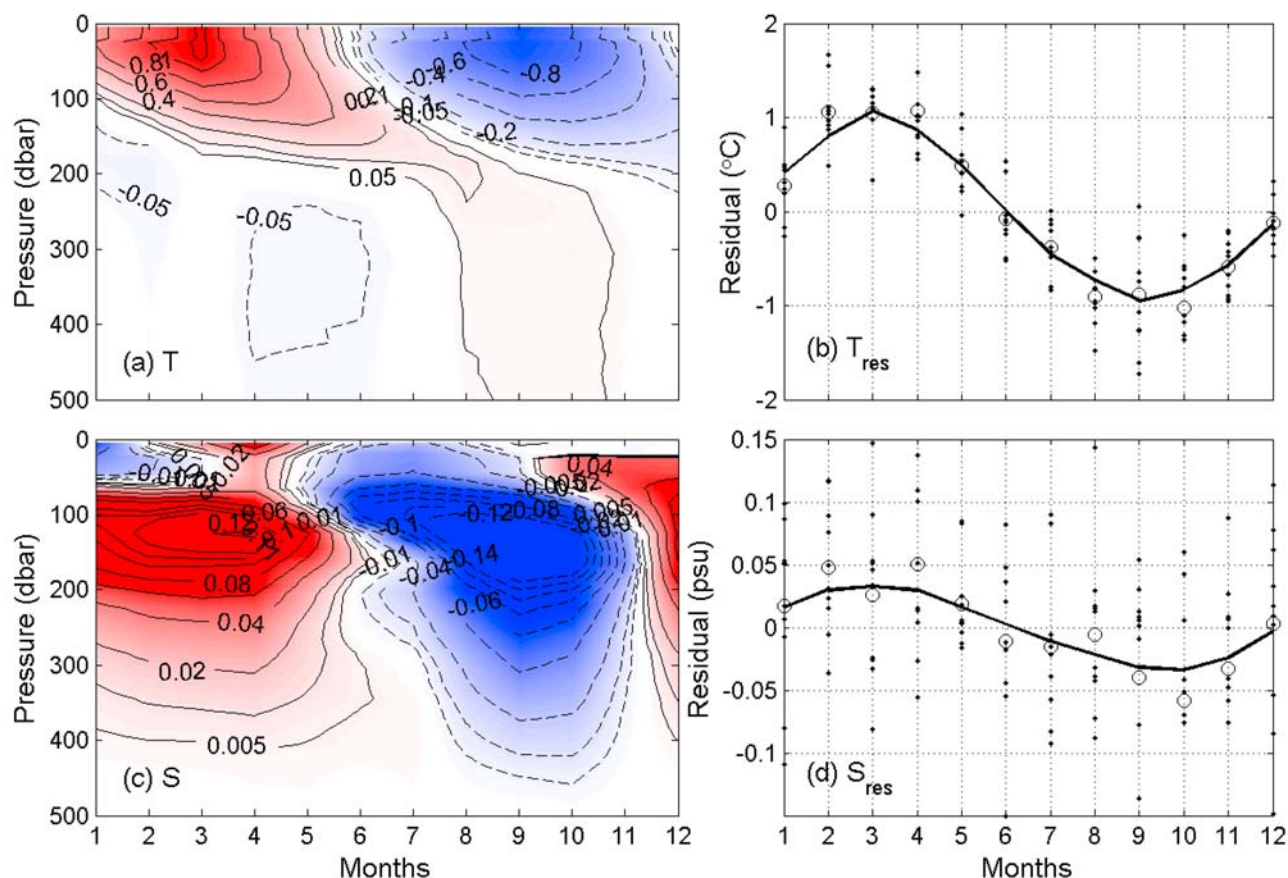
Figure 5. The annual march of (a) temperature and (c) salinity anomalies are deduced from available float data for the ACC region. The temperature plot represents the annual march over the whole latitudinal band (40–60°S), while the salinity plot represents the latitudinal range between 56 and 58°S. The mean seasonal residuals between 0 and 100 dbar of (b) temperature and (d) salinity are plotted for each latitudinal zone using black dots. Circles in Figure 5b represent the mean of the residuals represented by the black dots, and in Figure 5d they represent the mean residuals between 100 and 200 dbar in the latitudinal range 56–58°S. A 3 month running mean is applied to the data (solid line) to filter out any interseasonal noise existing in the data.

measurements of temperature and salinity at each station during the second GH CTD section. Note that prior to calculating the GEM-derived temperature and salinity profiles, the GEM fields were recalculated by excluding the observed section in order that the profiles be independent of the directly measured data. The GEM-derived profiles were then plotted using the spatial coordinates (longitude, latitude) of the original CTD stations (Figure 6) and can be compared to the directly measured section in Figure 2. A number of hydrographic structures in the GEM-reproduced temperature and salinity sections compare closely with those found in the observed data. Features, such as the fronts, the thermocline depth and the temperature minimum layer, are very similar to the observed sections. The axial positions of the STF, SAF and APF in the GEM fields are within approximately 30 km of the observed positions. The GEM reconstructions do tend to filter out small-scale features, such as the isolated 2°C isotherm located at 52°S in the observed data. However, an anticyclonic anomaly can still be seen in the GEM fields at 50°S, although its intensity is somewhat reduced compared to the observed data sets.

On the other hand, the core of an anticyclonic feature, observed at 42°S during the first GH CTD section, is exaggerated by the GEM fields (not shown), while the structure of an anticyclonic feature, crossed between 38 and 40°S [*Gladyshev et al.*, 2008], has been remarkably well represented by the GEM even though this feature is found outside the domain of the ACC and where information of the thermohaline properties and dynamic heights do not exist in the original GEM relationships. As the errors are largest in this region, we are unable to explain why this particular feature is well represented in the GEM fields as it does not occur on the norm. The RMS residuals of temperature and salinity (Figure 6) are mostly confined to the upper 300 dbar, where uncertainties in the mixed layer are greatest due to seasonal changes and the interaction between the atmosphere and upper ocean. Additionally, the inability of the GEM to reproduce the exact depth of the capped temperature minimum water south of the APF in early summer, leads to some increased subsurface residuals in temperature and salinity in the southern parts of the section. The increased residuals in the upper mixed layer are clearly
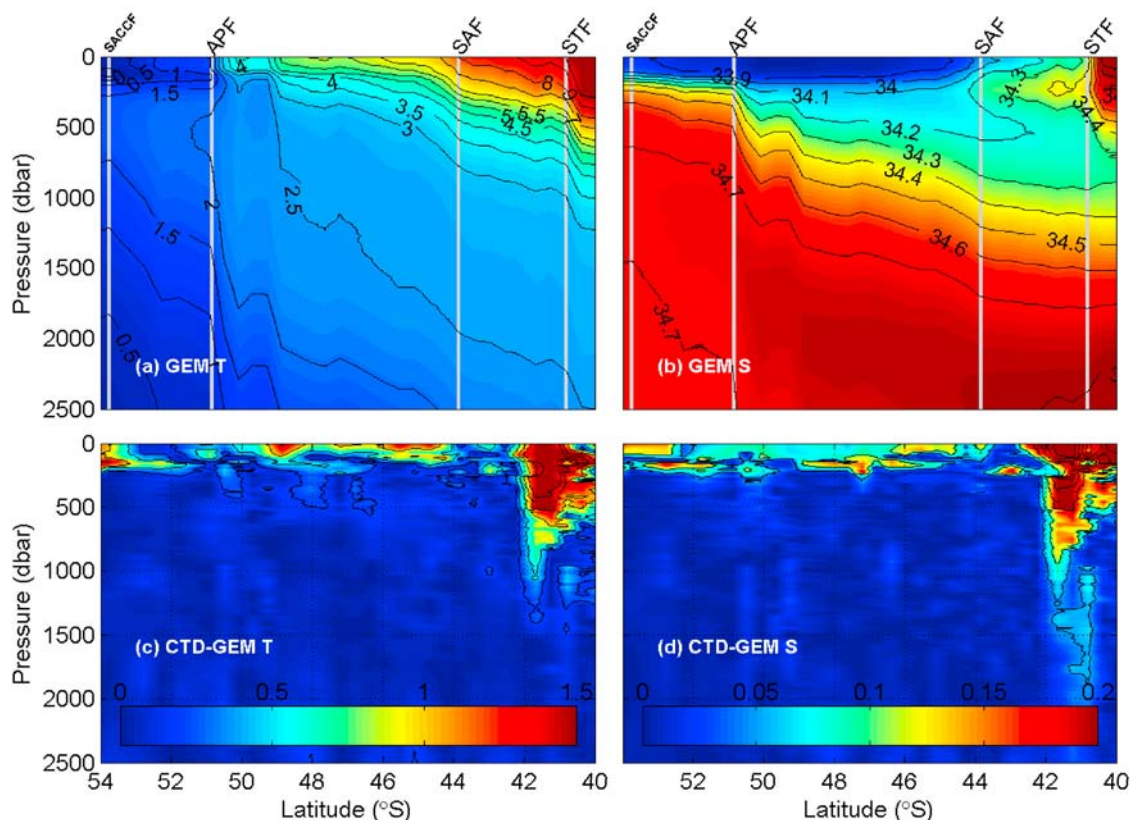
Figure 6. GEM-estimated sections of (a) temperature and (b) salinity pertaining to the CTD dynamic height data from the second GH occupation. The ACC front locations, as determined using the criteria of *Orsi et al.* [1995], are indicated by the vertical grey lines. The RMS difference between the in situ CTD and GEM-produced sections are shown for (c) temperature and (d) salinity, in °C and psu, respectively.

identifiable in the residual plots south of Australia, by *Sun and Watts* [2001]. The residuals in both studies increase toward the northern latitudes, however, at the GH line, the increase is more abrupt and localised in the northern SAZ where the shape of the deepening residuals clearly represents the presence of mesoscale eddies in the section. The subsurface errors in the *Sun and Watts* [2001] study extend deeper (1500 dbar) than those south of Africa (sudden decrease in residuals at ∼250 dbar).

[25] To assess the accuracy of the GEM at representing the "true" temperature and salinity properties of the ACC, we conduct the same examination process as *Watts et al.* [2001], which calculates the percentage of the hydrographic variance that is captured by the GEM fields (Figure 7). The variance is represented as

$$variance(p) = 1 - \frac{\sigma_{res}^2}{\sigma_{hyd}^2}, \qquad (1)$$

where σ_{res}^2 is the variance of the residuals in the GEM fields and σ_{hyd}^2 is the total variance of the hydrographic sections. The percentage of variance captured in each property increases quickly with pressure and shows improvement in the layers least affected by surface forcing and seasonality (below the thermocline). On average, up to 94% of the temperature and the density, and 85% of the salinity variance is captured by the GEM in the upper 500 dbar. This

increases sharply to 99%, 95% and 98% for temperature, salinity and density, between 500 and 2500 dbar, respectively. The ratio between the low observed variance of the deeper water masses (like Circumpolar Deep Water) and constant GEM residual variance causes the salinity and density variance captured to decrease in the deeper levels (1500 dbar). This was similarly noted south of Australia [*Sun and Watts*, 2001], where the minimum variance captured by the salinity occurs slightly deeper (2000 dbar) than in the African sector. In this study, the captured salinity variance in the upper layers is much lower (∼80%) than the estimates made by *Sun and Watts* [2001] at the SR3 transect (∼96%). The disproportionately high difference in ACC water mass salinities from those of subtropical origins introduced in the SAZ may cause some of the lower captured variance in the upper 1000 dbar, as the GEM struggles to represent the water mass properties with accuracy. The mean variance captured by the GEM, through the entire water column, is shown for each property, in Figure 7.

5. Applying Satellite Altimetry to the GEM

5.1. A Time Evolving Absolute Dynamic Topography

[26] To investigate the possibility of extending the temporal range and resolution of the GEM, we apply an altimetry derived absolute dynamic topography (ADT) data
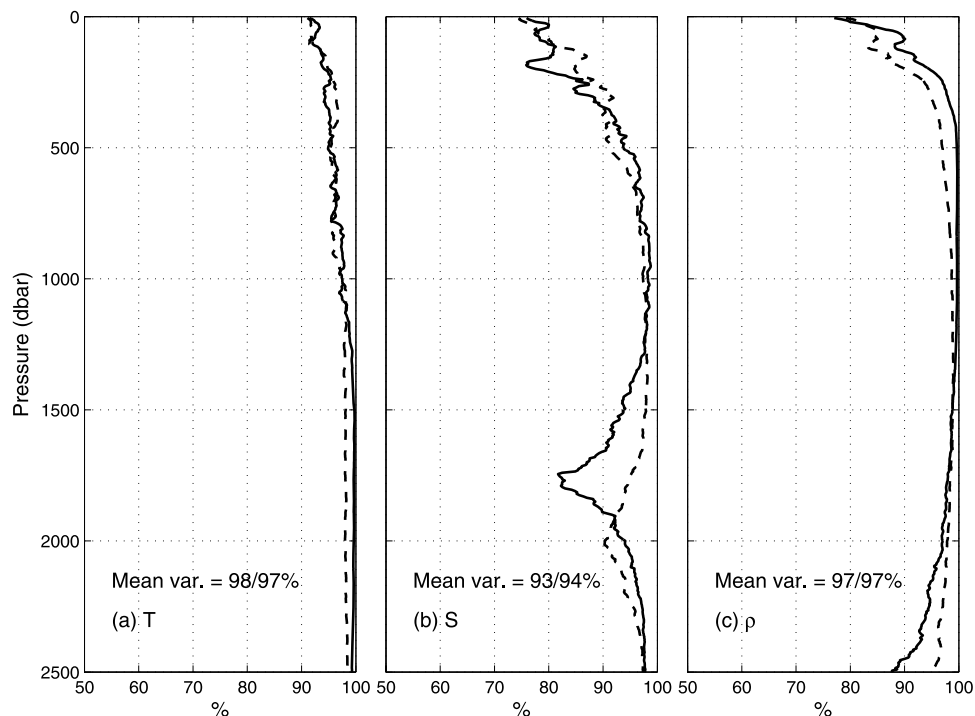
Figure 7. Percentage of hydrographic data variance captured by the GEM (solid curves) and AGEM (dashed curves) fields of (a) temperature, (b) salinity, and (c) density. The mean variance captured through the water column is displayed for the GEM and AGEM, respectively.

set to the empirical GEM relationships. The ADT is produced by adding a mean dynamic height state, created from repeat hydrographic sections at the GH line (see *Swart et al.* [2008] for further details), to altimeter SSH anomalies. The ADT is representative of the entire water column and therefore, may additionally reflect both changes in the density field below 2500 dbar and a barotropic component. One cannot ignore supplementary errors introduced by temporal and spatial sampling discrepancies and interpolation, mapping errors and tides not entirely removed from the altimeter signal. Despite these factors, the ADT data are very similar to the hydrographic estimates of dynamic height (mean RMS error is 0.063 dyn m, from *Swart et al.* [2008]). This suggests that the ADT largely reflects baroclinic changes in the upper 2500 dbar of the water column.

[27] Altimetry GEM (AGEM) is the name we assign to the product that combines the ADT data with the GEM empirical relationships. The primary reason for creating the AGEM rests in the fact that data time series in the Southern Ocean, and particularly in the African sector, are so rare. To date, the large majority of ship board observations take place solely in the austral summer months. Profiling float data are helping to address this problem, however, profiles remain scarce when compared to the vast expanse of the Southern Ocean. For the first time, the AGEM is able to provide information on the subsurface baroclinic structure of the ocean at eddy resolving spatial and temporal scales.

[28] Before this continuous time series of ADT data are used to render time evolving profiles of temperature and salinity, we accurately delineate the ACC front positions in space and time.

5.2. Positioning the ACC Fronts Using Satellite Altimetry

[29] Given that the ACC, south of Africa, is unbounded by any continental landmasses, its ocean boundaries or fronts have to be accurately defined using remote sensing techniques. In recent studies, high-resolution hydrographic and satellite sampling have been able to accurately locate the ACC fronts in space and time [*Sokolov and Rintoul*, 2002, 2007a, 2007b, 2009a, 2009b]. *Swart et al.* [2008], briefly describe the use of altimetry data and in situ data to identify the ACC frontal zones, along the GH line. Previously, we have described that altimetric SSH data are largely representative of the maximum baroclinic shear in the water column. This means that regions of increased horizontal gradients in dynamic height are representative of the local maximums in the baroclinic shear and therefore, associated frontal jets or branches.

[30] The mean meridional gradient in MADT data, along the GH line, reveals the dominant frontal regions (Figure 8). In the mean gradient, the SAF is represented by one core front (at 44.4°S), followed by two distinct branches of the APF, located at 48.9°S and 50.5°S. Further south, the SACCF is located at 53.5°S and the SBdy of the ACC is located at 55.6°S. An additional branch of the SAF, not shown in the mean MADT gradient, is sporadically present in time, south of the core SAF (seen on a portion of the MADT gradient plots and located, on average, at ~48.2°S). On occasions, this branch may merge with the northern branch of the APF, located on average, just 87 km to the south (identified in mean plots of MADT geostrophic velocities and MADT eddy kinetic energy of the region). The mean gradient in dynamic height related to the main
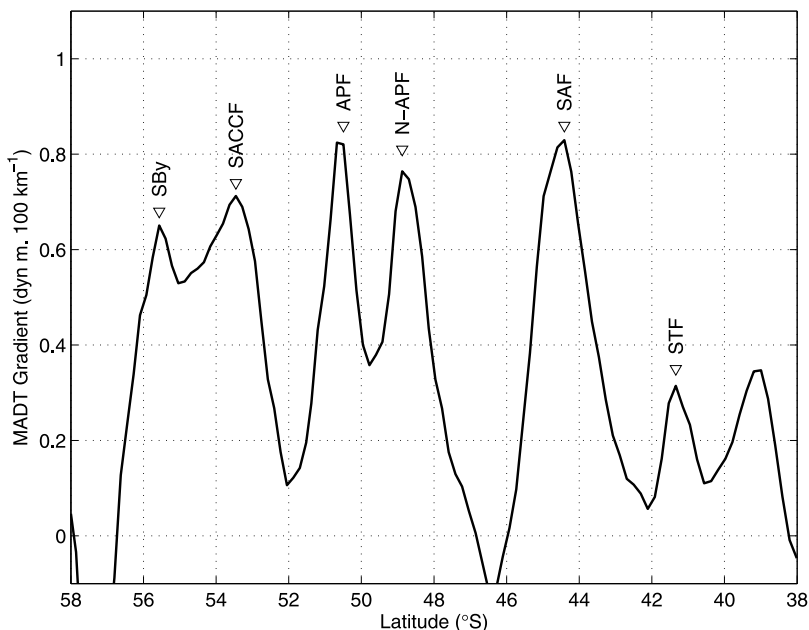
Figure 8. The mean MADT gradient (in dyn m 100 km^{-1}), at the GH line, marks the positions of the ACC fronts (marked and labeled).

branch of the SAF and the APF is approximately 0.8 dyn m per 100 km, while due to the reduced intensity of the southern ACC fronts, the gradients over the SACCF and SBdy are ∼0.65 dyn m per 100 km. The northernmost peak in the MADT gradient may be associated with the northern branch of the STF, but it is not constantly present in time because it is made of a continual stream of cyclones and Agulhas Rings originating at the Agulhas Retroflection [*Belkin and Gordon*, 1996; *Swart et al.*, 2008; Dencausse et al., submitted manuscript, 2009]. The position of these fronts can be compared to the meridional distribution of the ACC's baroclinic transport, represented in latitudinal bins along the GH line, and given by *Swart et al.* [2008].

[31] Similarly to the principles of the GEM, the conservation of streamlines means values of dynamic height will coincide with constant water mass properties and thus fronts. Like *Sokolov and Rintoul* [2002, 2007a], we examine the distribution of the MADT gradient at the GH line and find that constant values of MADT (streamlines) match localised MADT gradient maximums. The location of these gradient maximums and associated isolines of MADT are very similar to the front positions located in hydrographic data and defined by the *Orsi et al.* [1995] criteria (i.e., the major front cores at the GH line match the definition provided by *Orsi et al.* [1995]). We adapt the mean dynamic height in 5 year periods, between 1992 and 2008, in order to take into consideration the temporal variability in dynamic height space that might occur over the 16 year time series. The mean fixed values of MADT that have been used to locate the fronts, as well as their mean positions and standard deviation, can be found in Table 2.

[32] To test the consistency of using this method, we overlay the fronts position onto the MADT velocity magnitude ($\sqrt{(u^2 + v^2)}$; Figure 9). The fronts consistently follow the highest velocity magnitudes induced by the baroclinic shear of the fronts. Furthermore, Figure 10

provides a representation of the frequency at which the altimeter-derived fronts match the localised MADT gradient maximum associated with the front for the whole altimetry time series (1992–2008). Apart from the STF, the fronts are found at the exact position or within 0.2° latitude (20 km) of the maximum gradient between 52 and 73% of the time. Of these fronts, the worst performers are the two southernmost fronts (SACCF and SBdy), which is likely due to their weaker gradients, thus making it harder to "pinpoint" their exact location. However, none of the main ACC fronts are found more than 2° latitude away from the maximum gradient. As expected, the STF is the worst performer with only 3% of the front positions matching the exact location of the maximum gradient and over 28% of the time the front position is located over 2° latitude away. It must be noted that these inaccuracies are exaggerated because (1) Agulhas Rings and other mesoscale features found just north of the STF cause large MADT gradients that dominate the generally weaker true frontal gradients and (2) because the latitudinal range of the STF overlaps the latitudinal range of the SAF by ∼1° latitude. This means that in some cases the maximum MADT gradient is incorrectly associated with the SAF and not the STF, thereby resulting in higher inaccuracies. The STF is generally a weaker front than the

Table 2. Mean Value of MADT, Used to Follow the Fronts in the MADT Time Series, as Well as the Mean Latitudinal Position of Each Front and Their Standard Deviations Are Listed

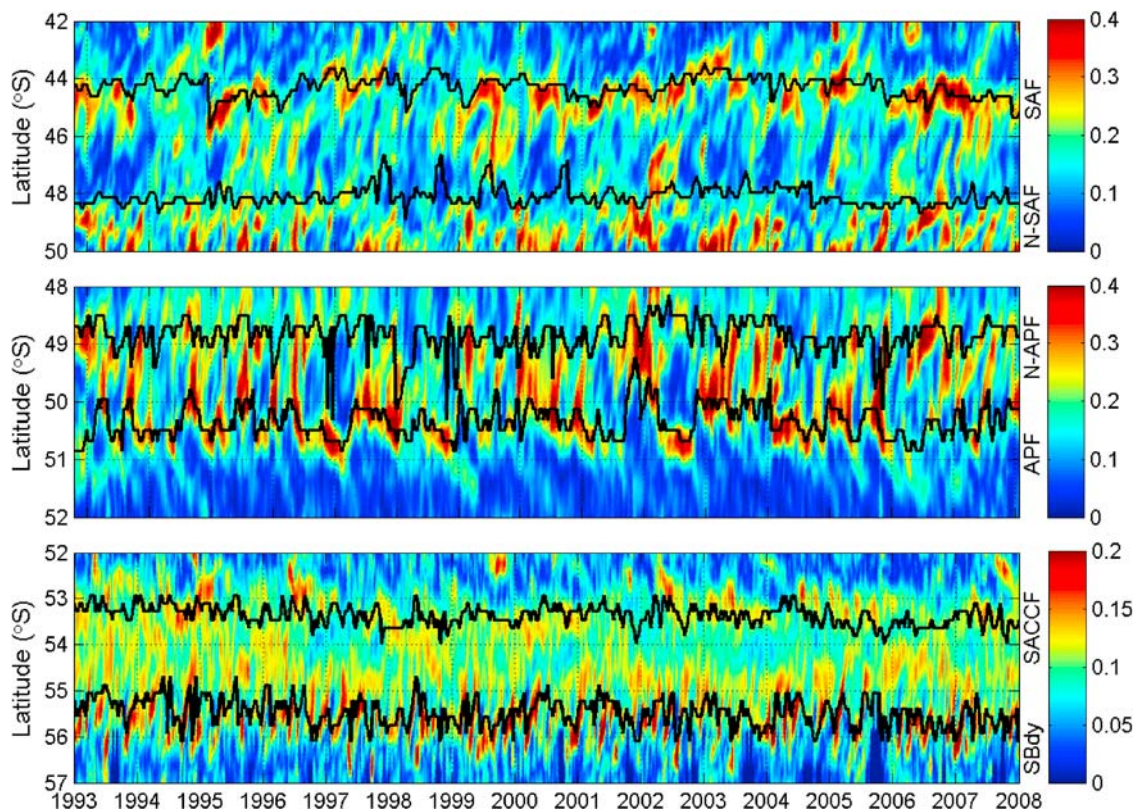| Front	Mean MADT (dyn m)	Front Position (°S)	Standard Deviation (° latitude)
STF	1.41	39.9	1.51
SAF	1.15	44.3	0.36
APF	0.49	50.4	0.27
SACCF	0.18	53.4	0.21
SBdy	−0.07	55.5	0.32

Figure 9. The positions of the ACC fronts, determined using the methods described in section 5.2, are overlaid (black curves) on the MADT velocity magnitude (color plot; in m s^{-1}) at the GH line.
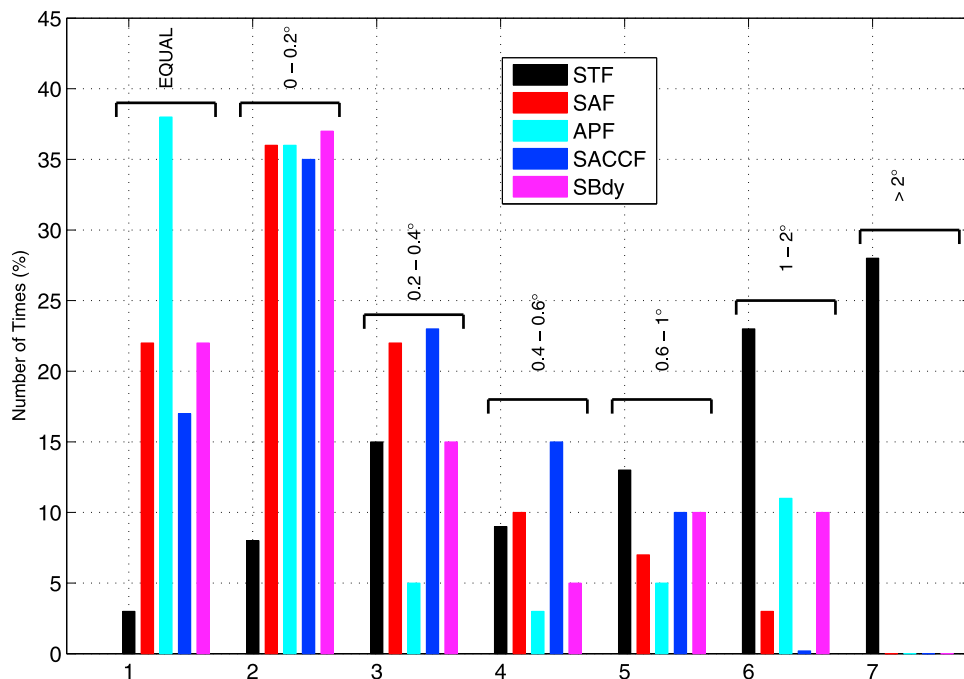

Figure 10. The frequency (in %) of categorized distances between the position of the MADT-deduced ACC front and the local maximum in the MADT gradient, expected to be associated with that particular front. The categorized distances are displayed.
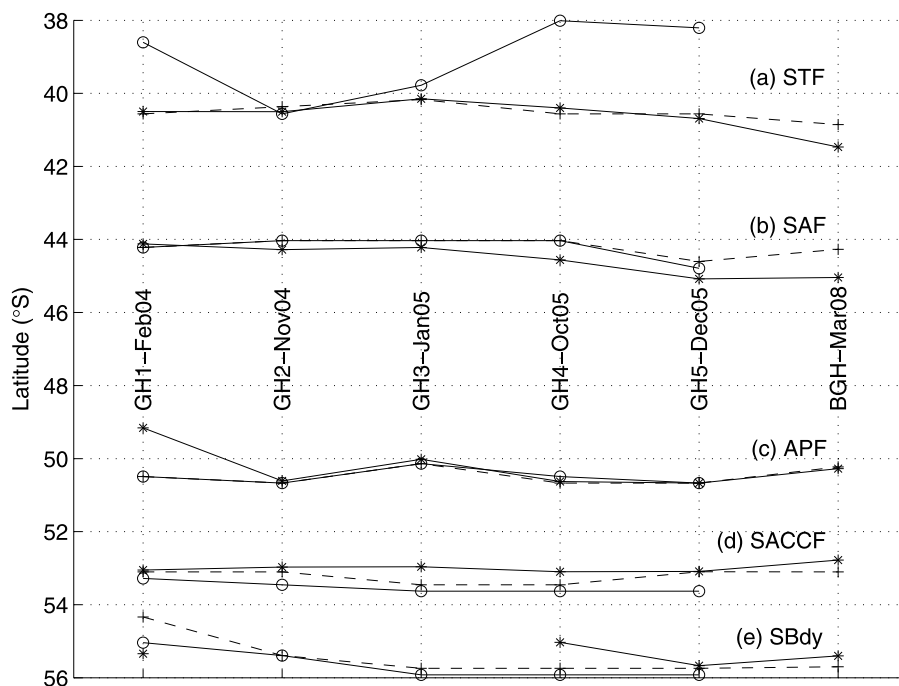
Figure 11. Latitudinal positions of the major ACC fronts determined from six repeat XBT occupations at the GH line (stars), from the AGEM-estimated temperature sections (crosses), and from satellite altimetry MADT data (circles).

SAF and so this form of error exaggeration is particularly true in this case.

[33] There are additional, yet smaller and less consistent jets present in the MADT velocity magnitude and gradient plots. Examples include the additional branches of the SAF and APF that are depicted in Figures 8 and 9. Comparatively, *Sokolov and Rintoul* [2002, 2007a] locate many more front branches south of Australia (e.g., 3 SAF branches, 2 APF branches, and 2 SACCF branches) than seem to be present in the African sector. This is partially justified by the deeper topography found south of Australia (such as the Australian-Antarctic Basin), which would allow for increased front destabilisation and jet separation. However, a more in-depth analysis on the front structures south of Africa may reveal many more jets, but for the purpose of this study, we only require locating the major fronts of the ACC.

5.3. Comparing ACC Front Positions

[34] We now attempt to verify the frontal positions represented in the AGEM sections, using hydrographic sections. This indicates how accurately the AGEM represents the baroclinic boundaries in the ACC throughout the water column. The criteria used to locate the ACC fronts from the hydrography and the AGEM-produced temperature sections come from *Orsi et al.* [1995], and are the same fronts located by the localised peaks in the MADT gradient described in section 5.2 and shown in Figure 8.

[35] The positions of the ACC subsurface temperature fronts, from six GH XBT occupations, are shown in Figure 11. The position of the ACC fronts, determined using the AGEM temperature sections, as well as from the satellite altimetry (described above) are also shown in Figure 11 for comparison. No altimetry-derived front posi-

tions are available for the last hydrographic section because the MADT data were not yet available for that period. However, AVISO "near-real-time" altimetry data (released within 7 days), obtained during the cruise (BONUS-GH section) [*Speich and Dehairs*, 2008], were used to derive AGEM sections and the fronts positions, which allowed for comparison to the hydrographic front positions. (It must be noted that using the near-real-time altimetry data does not allow for the exact knowledge of the satellite orbit and therefore its precision is less accurate than the "delayed time" data. However, such precision was not necessary for use on the research vessel.) This was the first documented occasion the AGEM was used on a research cruise to accurately determine the subsurface position of fronts and the subsurface structure of mesoscale features prior to arrival with the research vessel. This allowed for optimal spacing of subsequent CTD and biogeochemisty sampling stations during the voyage.

[36] In Figure 11 the AGEM is for the most part effective at determining the latitudinal positions of the ACC fronts. Position matching, using MADT tracking, is least successful for the STF, where intense mesoscale variability and meandering in the front induces erratic meridional shifting. However, the AGEM still provides accurate positions when being compared with the in situ hydrographic positions. The AGEM positions of the SAF and APF are, on many occasions, the same as the MADT derived positions, which suggests the maximum gradients in the MADT are describing the subsurface temperature gradients correctly. On average, the SAF hydrographic front positions are found slightly further south than the two other methods. This may be caused by the fact that the subsurface expression of the front is not always found directly beneath the surface expression [*Lutjeharms*, 1985], causing a spatial discrepancy
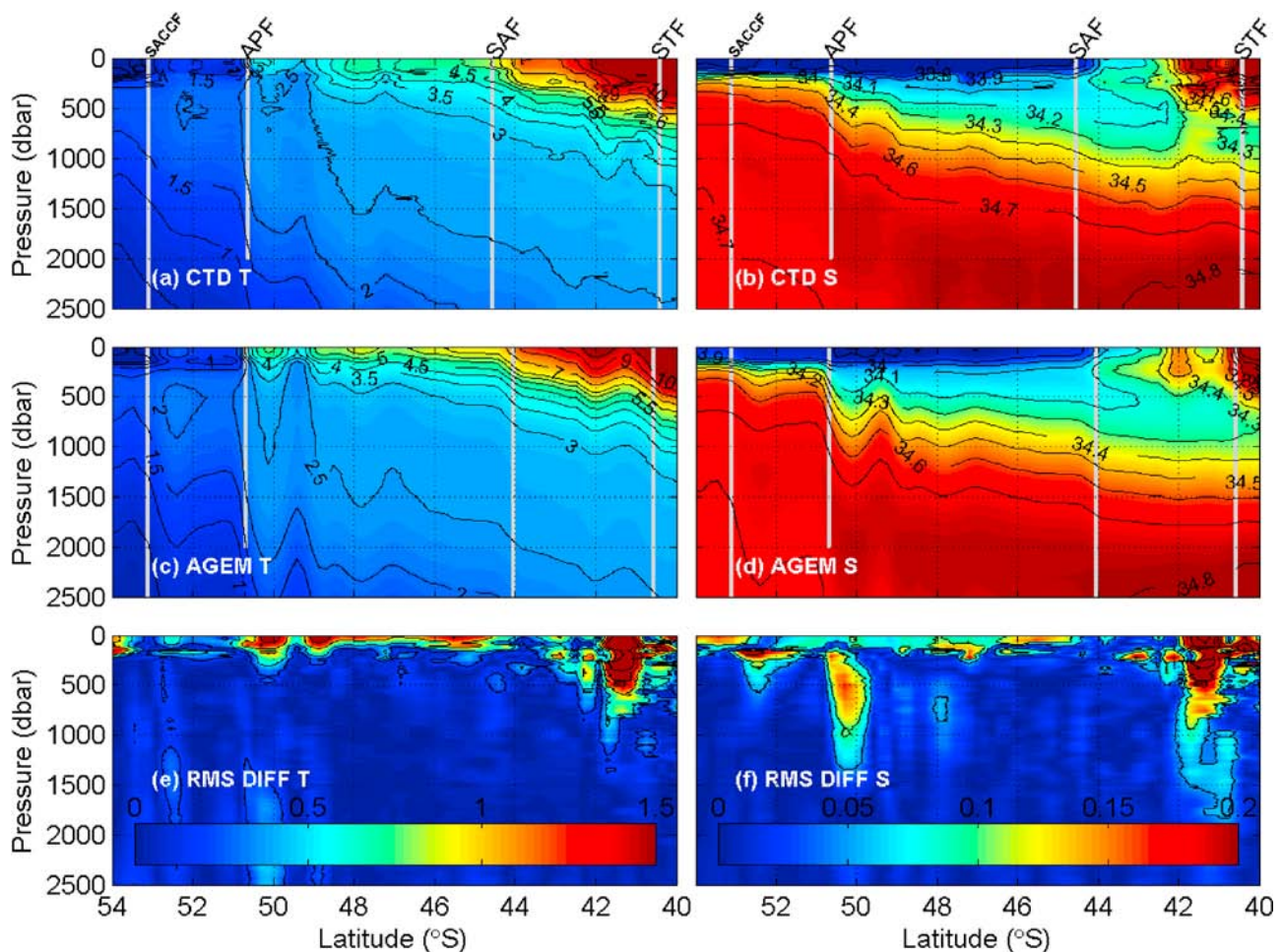
Figure 12. Comparison of the observed (a) temperature (in °C) and (b) salinity (in psu) sections with that of the AGEM-produced sections of (c) temperature and (d) salinity using solely the altimetry derived ADT data, from the time the observed section (second GH CTD transect) was carried out. The RMS difference between the observed and AGEM-estimated sections of (e) temperature and (f) salinity are displayed. The ACC front locations, as determined using the criteria of *Orsi et al.* [1995], are indicated by the vertical grey lines.

between the maximum gradient in the altimetry SSH signal and the maximum gradient in the subsurface temperature. The positions of the APF overlap with considerable accuracy (only 30 km separating the observed and AGEM positions and 35 km separating the observed and MADT position) using all three methods, albeit the first XBT occupation. The weak nature of the SACCF and SBdy lead to determining the positions with less accuracy using the AGEM and MADT tracking, compared with the more baroclinically "intense" SAF and APF. Furthermore, the fact that the SBdy was not reached during all the hydrographic transects, may lead to additional inaccuracies in determining its position using the AGEM. The SBdy was not reached during the second and third XBT occupations so we are unable to compare its observed position with the AGEM and MADT positions.

5.4. Validating the AGEM

[37] The 16 year time series of ADT data, described in section 5.1, are applied to the GEM empirical relationships to render time evolving profiles of temperature and salinity.

[38] To assess the ability of the AGEM method to capture the thermohaline structure of the ACC accurately, we compare the measured data with time coherent AGEM temperature and salinity profiles. It is important to note that in order to provide an independent validation, the CTD data that are being compared are withheld from the empirical relationships used to infer the thermohaline information. The temperature and salinity sections produced by the AGEM (Figure 12) at the time of the second GH occupation can be compared with the observed CTD sections in Figure 2. The AGEM-reconstructed sections are remarkably similar to the observed sections. All water mass boundaries are well represented and major mesoscale features are accurately captured by the AGEM. In particular, the depth of the thermocline is correctly placed. This is similarly the case for the extent of the salinity minimum layer and its progression with depth toward the north. The representation of some mesoscale features is also reproduced accurately. A weak anticyclonic feature, crossed just north of the APF, is "picked up" by the AGEM representations, although the AGEM does seem to exaggerate the strength of this feature to some extent.
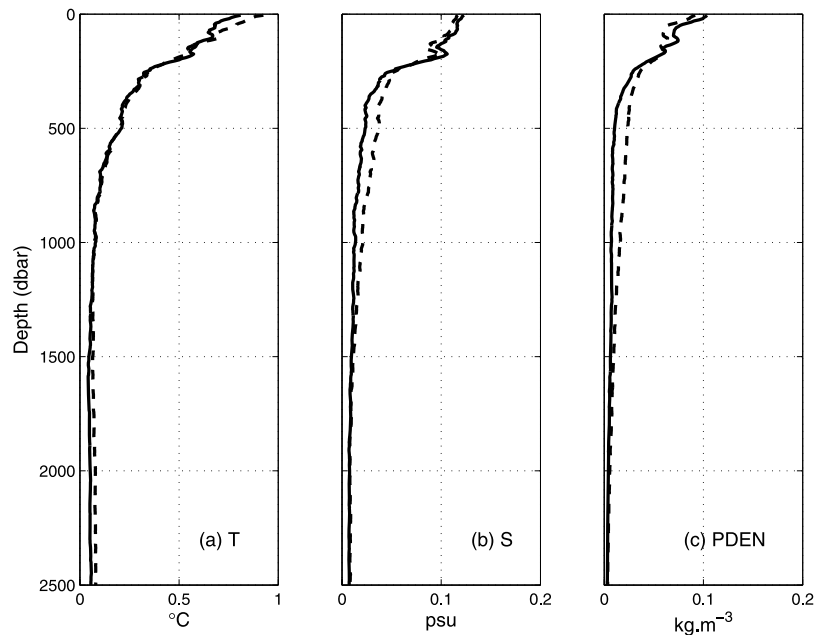
Figure 13. The mean RMS residuals between the GEM (solid curve) and the AGEM (dashed curve) and the in situ hydrography are compared for (a) temperature, (b) salinity, and (c) density.

Additionally, an isolated "patch" of warmer water, centered at ~52°S and 500 dbar pressure, is also represented by the AGEM temperature section. However, slightly higher temperatures and greater salinities are created in the upper 150 dbar layer in the AGEM sections. This is responsible for the broad band of errors found in the upper layer extending between the SAF and SACCF. The latitudinal distribution of errors are spaced out relatively evenly, except for north of the SAF. The AGEM is expected to introduce greater inaccuracies, north of the SAF, where different water masses extraneous to the ACC are introduced by mesoscale activity, causing the relationship between the dynamic height and temperature and salinity to become multivalued. Deeper residuals, located in the southern parts, are sporadic in nature (associated with an anticyclonic feature already mentioned) and are not found in the mean distribution of error with depth.

[39] The RMS of the residuals between the GEM and AGEM estimates and the in situ hydrography, for all the CTD stations used in this study, is summarized in Figure 13. In both methods, larger residuals are found in the upper 300 dbar, where seasonal and atmospheric effects increases the variability. The residuals decrease sharply for all properties, below the thermocline. The AGEM residuals are, on average, greater than those of the GEM. It is likely that sampling errors (see section 5.1) introduced in the ADT data, when compared with in situ CTD derived dynamic heights, cause these higher residuals, especially between 300 and 1500 dbar for salinity and density. The higher residuals in the deep layers are not entirely caused by altimeter sampling errors but more due to the combination of the following two factors. The first factor is due to the very nature of the GEM projection, which removes a large fraction of the temporal variability associated with transient features, such as smaller-scale mesoscale eddies [*Sun and Watts*, 2001]. This is especially evident in the northern

domains of the ACC, where deep mesoscale features (Agulhas Rings) invade the SAZ. This variability is captured by the satellite altimeter and the error is projected to the deeper layers. Additionally, the ACC front positions vary more extensively in the northern domains. These variations are associated with at the least the upper 2000 m of the water column and therefore these changes are incorporated in the altimeter signal. The few CTD sections used to construct the GEM limit the extent to how much of this variability is captured in the GEM fields. The second factor is that the altimetry data includes the barotropic signal of the water column, which may cause additional error in the deeper layers by computing the AGEM-derived temperature and salinity baroclinic changes without the barotropic component. In the upper 500 dbar, the mean errors for both the GEM and AGEM in temperature, salinity and density are 0.4°C, 0.06 and 0.04 kg m^{-3}, respectively. This is drastically reduced, by about ~80%, to 0.07°C, 0.015 and 0.08 kg m^{-3} for the same properties, between 500 and 2500 dbar.

[40] Similarly to the GEM, we calculate the hydrographic variance captured by the AGEM in Figure 7. Surprisingly, by comparing the GEM and AGEM in Figure 7, the AGEM, at many depths, performs better than the GEM. Although only slightly, the AGEM captures more of the variance in the upper thermal and salinity layers but under performs in the upper density layer. The variance captured in the deeper salinity layer (1000 dbar) performs better in the AGEM, where the percentage does not drop below 90%, while for the GEM, the variance captured drops to below 83% at ~1750 dbar. The better performance of the AGEM in the deeper layers may be caused by the AGEM capturing a greater portion of the mesoscale variability (due the high spatial and temporal resolution of the altimetry data set), found predominantly in the northern ACC domains, compared with the CTD-derived GEM fields. This is enhanced
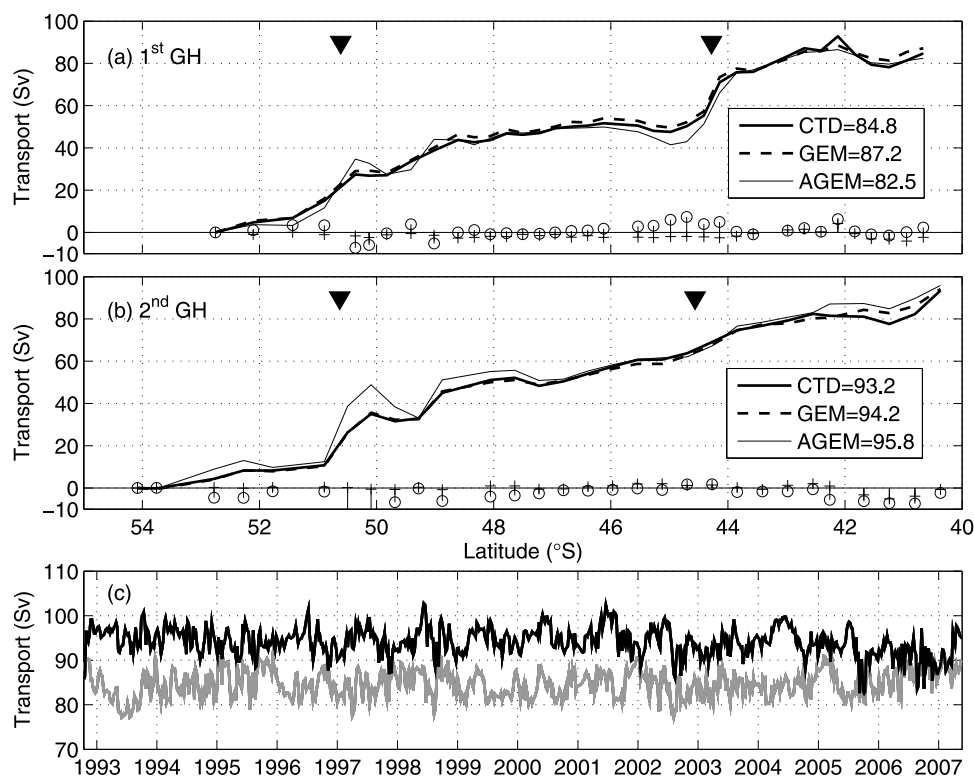
Figure 14. Comparison between accumulated baroclinic transports of the ACC, estimated from the (a) first and (b) second GH CTD occupations (thick curves), those estimated using the GEM-estimated sections (dashed curves), and AGEM-estimated sections (thin curves). The difference between the GEM and hydrographic estimates (crossed tick marks) and the AGEM and hydrographic estimates (circled tick marks) are displayed along the x axis. The hydrographic latitudinal positions of the SAF and APF are marked by right and left arrows, respectively. (c) The AGEM-derived net accumulated transports for the ACC (black curve) are compared with the estimates made by *Swart et al.* [2008] (grey curve).

in the deeper layers by the mesoscale features, which easily extend to over 2000 m deep. On average, up to 95% of the temperature, 86% of the salinity and 91% of the total variance is captured by the AGEM in the upper 500 dbar. Again, the percentage increases sharply below the thermocline (500–2500 dbar) to 97% for the temperature and density, and 94% for the salinity variance.

5.5. A Baroclinic Velocity Field Created Using the AGEM

[41] A sound method in which to test the performance of the GEM and AGEM is to relate its reproduced sections to the geostrophic velocity equation, which can assess whether the reproduced fields have correctly determined the baroclinic shear. This is done by comparing the GEM and AGEM velocity fields at depth and the total transport of the ACC, along the prime section upon which the GEM is built (GH line), to observed velocities and volume transports.

[42] First, we compute the total accumulated baroclinic transport of the ACC from the two CTD occupations of the GH transect with the GEM and AGEM-reproduced transports (Figures 14a and 14b). The transports are computed relative to 2500 dbar and accumulated from the SBdy to the STF, as determined using the criteria of *Orsi et al.* [1995], from the CTD sections. Again, in order to provide an independent validation, the CTD data that are being com-

pared, are withheld from the empirical relationships when deducing the GEM temperature and salinity sections.

[43] A general description of the accumulated transport shows that the main gains in transport are over the ACC fronts, particularly the SAF and APF (located on Figure 14a and 14b using arrows). The transport curves produced by the GEM, AGEM and observed estimates follow each other closely. Eddy variations in the transports are captured by all three methods, however, these variations are exaggerated by the AGEM method. A reason for this may be the temporal and spatial sampling difference between in situ dynamic heights and those derived using altimetry data. For example, the difference in sampling an eddy at its core or at its edges may lead to small differences in the calculated dynamic height that can lead to differing baroclinic transport curves. This is particularly evident in the transport curves (Figure 14b) due to the "eddy-like" feature that was crossed just north of the APF (~50°S) in the second GH CTD occupation (see Figure 2). Due to this anomalous feature, the maximum difference between the observed transport and the AGEM-derived transport reaches up to 15 Sv. In addition, higher AGEM transports may, in part, come from the SSH signal that includes a barotropic component, which we are yet unable to isolate due to a lack of information about the Earth's geoid [*Swart et al.*, 2008]. The difference in baroclinic transport between the CTD
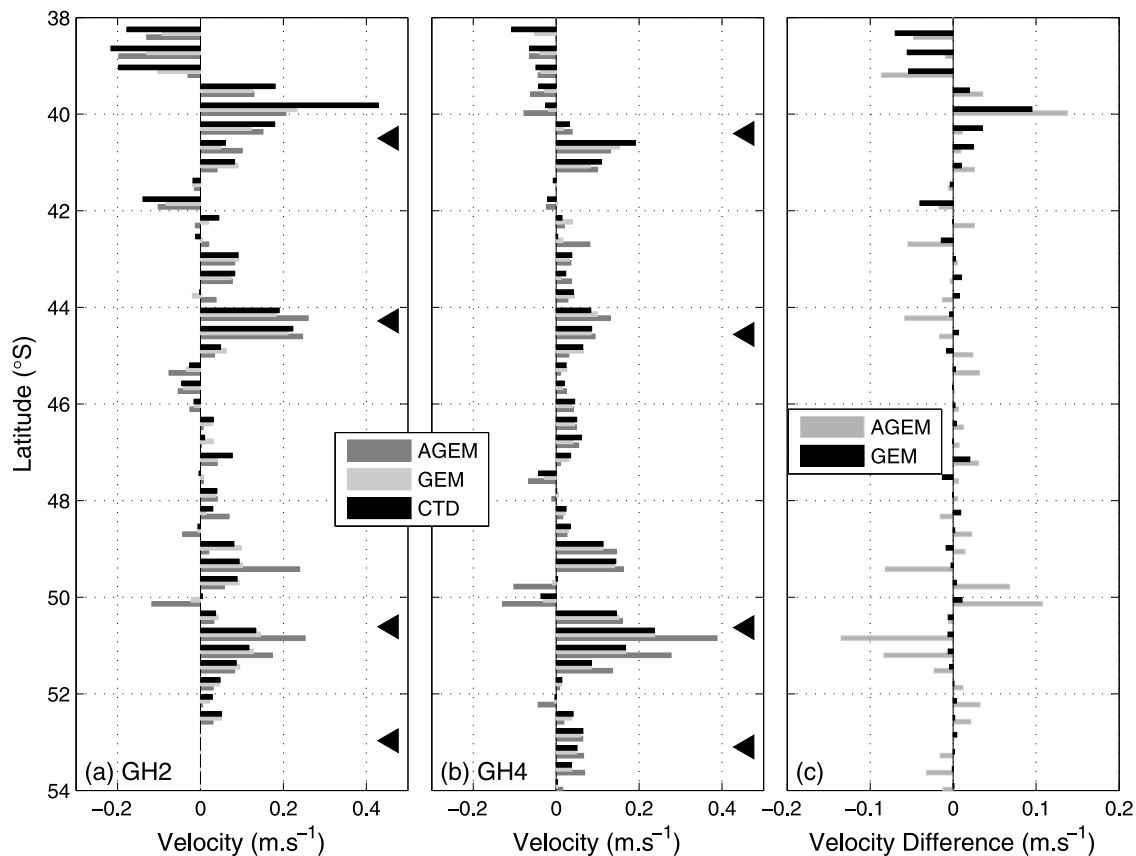
Figure 15. The cross-sectional velocities at 300 dbar (in m s^{-1}), estimated from the (a) first and (b) second GH CTD occupations (black bars) are compared with the velocities estimated from the GEM- (light grey bars) and AGEM-derived (dark grey bars) sections. The latitudinal positions of the ACC fronts, determined from the CTD temperature sections are indicated from top to bottom as follows: STF, SAF, APF, and SACCF. (c) The mean velocity difference between the CTD-estimated velocities and those estimated from the GEM- and AGEM-derived sections are summarized.

estimates, and the GEM (crossed tick marks) and AGEM (circled tick marks) estimates are indicated along the x axes in Figures 14a and 14b. The largest differences are found in the AGEM estimates, mostly near the fronts where eddy activity is greatest (mean RMS difference is 2.9 Sv). Small differences, seldom exceeding 2.5 Sv (mean RMS difference is 1.4 Sv) are found between the in situ and GEM transport curves. The overall differences between the methods are cancelled because the integrated transport over the ACC depend only on the end points, while the net transports are within 1−2.6 Sv of eachother. The end transports are given in Figures 14a and 14b and average 84.8 Sv and 94.4 Sv for the first and second occupation, respectively.

[44] The AGEM-derived accumulated baroclinic transports are extended to the whole ADT time series and compared to the accumulated transports taken from *Swart et al.* [2008] who use a different approach (Figure 14c). The *Swart et al.* [2008] transport time series is estimated by exploiting an empirical relationship between the dynamic height (relative to 2500 dbar) and the accumulated baroclinic transport of the ACC from regional CTD sections and applying the ADT data at the GH line to this relationship to render continuous transport estimates. Both transport esti-

mates are accumulated between the SBdy and the northern limit of the SAF (see *Swart et al.* [2008] for more details on front limit determinations) in order to eliminate the large variability and associated errors found in the region of the STF. The AGEM-derived net transports average 94.2±3.1 Sv, which is roughly 10 Sv higher than the estimates made by *Swart et al.* [2008] (84.7±3 Sv). In the study by *Swart et al.* [2008], the empirically derived transports were often ∼8 Sv lower than the CTD-estimated transports. This means that the higher AGEM transport estimates are likely more accurate than the *Swart et al.* [2008] estimates when compared to the true CTD estimates. Although the scale of variability between the two estimates is approximately the same, the short-term variations in the transports are not very similar. These differences are likely caused by the more basic structure of the empirical relationship used in the study by *Swart et al.* [2008], which may fail to record a portion of the smaller spatial scale variations in the accumulated transport. Nonetheless, in time, further transport comparisons may help us to understand the complex nature of the ACC flow in space and time.

[45] Secondly, the cross-sectional velocities, at 300 dbar, as deduced from the three methods, are shown in Figures 15a and 15b. For clarity, the three velocity estimates are offset
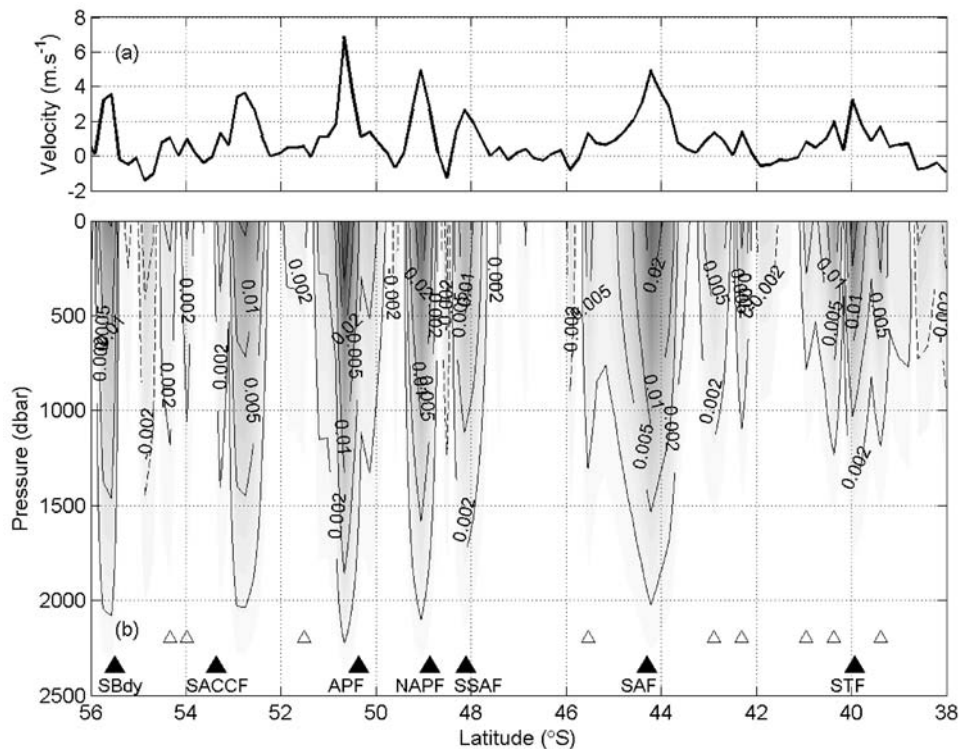
Figure 16. (a) The sum of the time-averaged (1992–2008) latitudinal distribution of the cross-sectional velocities (in m s^{-1}) at the GH line. (b) The vertical distribution of the cross-sectional velocities (in m s^{-1}) are depicted at the GH line. The large arrows show the mean positions of the major ACC fronts, identified by the ADT, while smaller arrows show those additional jet-like structures that are not clearly seen in the MADT velocities, presented in Figure 9.

from one another in Figure 15. Similarly for the baroclinic transports, the highest zonal velocities occur over the ACC fronts, indicated on Figure 15. In most places, the fine velocity structures compare closely with one another in space. The mean RMS difference between the observed and GEM-produced velocities is only 0.01 m s^{-1}. This error increases to 0.03 m s^{-1} between the observed and AGEM-produced velocities. The mean differences in the two methods for both GH occupations are summarized in Figure 15c. The highest errors are again located over the front regions, where eddy activity is higher and a large addition in error is attributed to the mesoscale feature crossed during the second CTD occupation along the GH transect, as discussed above. On two occasions in the first GH occupation, the AGEM transports within the ACC are approximately twice as large as the observed transports. Out of the ACC domain (north of ∼40°S), the errors increase due to the introduction of water masses that are characterized as having different T-S to dynamic height signatures, compared to those found in the ACC.

[46] Finally, Figure 16 shows the 16 year mean structure of the zonal velocities along the GH transect deduced from the AGEM sections. Several well-defined velocity cores are identified across the span of the ACC. These core jets are closely associated with the mean positions of the main ACC fronts identified in section 5.2 and indicated by the labeled arrows in Figure 16. The position of additional smaller velocity cores can be identified in the mean velocity field

and are represented by small arrows in Figure 16. The velocity cores of the SSAF and NAPF (briefly mentioned in section 5.2) can also be clearly made out. We are unable to identify the smaller cores in the mean MADT and velocity magnitude distribution plots in section 5.2, however, they exist in the mean AGEM velocity field. The southern jets are, in some places, interspersed with velocity reversals that may be associated with eddy velocity reversals due to eddy genesis taking place near the fronts. This representation emphasizes the strength of the main ACC fronts that, on average, extend to pressures greater than 2000 dbar. The deepest reaching front is the APF, where mean velocities are greater than 0.8 cm s^{-1} and often the velocities exceed 1.5 cm s^{-1} at 1500 dbar. The smaller velocity cores are considerably weaker and do not extend far beyond 1000 dbar in pressure.

[47] A future study will make use of the AGEM to zonally expand the velocity field to include the meridional velocity component. This will be able to help answer questions related to meridional exchanges of heat and freshwater in the Southern Ocean.

6. Summary

[48] Major current systems, such as the ACC, experience high temporal variability, yet the dominance of the GEM in these systems illustrates that thermohaline fields are remarkably organised in streamfunction space, as previously shown by *Book* [1998], *Meinen and Watts* [2000], and

Sun and Watts [2001]. This gives us confidence in the GEM's ability to capture most of the system's variability.

[49] The ACC is well suited to exploiting the GEM method because each value of dynamic height is characterised by a particular T-S curve, thereby illustrating that source waters have undergone similar physical processes to arrive at a particular streamfunction [*Watts et al.*, 2001]. This becomes more complicated in confluence regions where different source waters advect and converge, supplying different thermohaline properties along the same vertical coordinate at different times. This is precisely what occurs in the northern domains of the GH line, where subtropical Agulhas waters enter the ACC system and supply warm, salty water masses to the cooler, fresher environment of the SAZ [*Gladyshev et al.*, 2008; *Swart et al.*, 2008; *Swart and Speich*, 2010; Dencausse et al., submitted manuscript, 2009]. This was previously noted south of Africa by *Sun and Watts* [2001] where, in the upper thermal layer, temperature residuals where more than twice that of those found in the Australia sector of the Southern Ocean.

[50] Despite these intrusions, the GEM-based correlations, produced from a large assemblage of hydrocasts, are sensitive to the variability and changes occurring within the region of interest, conserving all the thermohaline structures found in the hydrography and even capturing transient structures with small vertical scale. The GEM captures more than 96% of the hydrographic variance below the thermocline. The RMS error in the upper 300 dbar for temperature and salinity are $0.54°C$ and 0.09, respectively. This decreases to, on average, $0.07°C$ and 0.02 below the thermocline. The GEM has shown its strength at determining, with great accuracy, the locations of maximum baroclinic shear and hence the positions of the ACC fronts. This is further tested by comparing baroclinic transports and velocities with pressure, which shows that the GEM methods produce closely comparable end transports of the ACC and the RMS errors in the velocity field, at 300 dbar, are less than 0.01 and 0.03 m s^{-1} for the GEM and AGEM, respectively.

[51] The extensive time series of altimetry data have to be more readily exploited in the Southern Ocean, where in situ data are so sparse and sampling is limited to the austral summer months. The combination of satellite altimetry data to the GEM greatly improves the spatial and temporal sampling resolution of the region, while giving us much needed insight into the time-varying subsurface structure of the ACC. In Part 2 of this study, the continuous time series of thermohaline fields are used to estimate the heat and salt content variability at the GH line and therefore the physical processes that dominate the behavior of the ACC. These estimates provide insight into the subsurface thermohaline variations of each ACC front and frontal zone, which previously has not been undertaken at such high spatial and temporal resolutions.

[52] The Argo float program is for the first time providing relatively good spatial coverage in the Southern Ocean. In time, these combined with hydro casts, will provide a large quantity of T-S profiles, which will greatly enhance the use of the GEM in all regions of the Southern Ocean and allow for extensive testing of numerical ocean models, that presently have little data to perform validations on.

[53] The combination of the AGEM sections and velocities, and the positions of the ACC fronts and spatial boundaries, defined using altimetry data, provides a powerful scientific tool toward improving our understanding of the variability occurring within the ACC. The accuracy of the AGEM to reproduce subsurface thermohaline conditions serves as a catalyst to further studies that utilize time series analysis [e.g., *Swart and Speich*, 2010]. The 16 year time series of AGEM observations will also allow for statistical decomposition of variance signals found in these results.

References

Ansorge, I. J., S. Speich, J. R. E. Lutjeharms, G. J. Goni, C. J. Rautenbach, W. Froneman, M. Rouault, and S. Garzoli (2004), Monitoring the oceanic flow between Africa and Antarctica, *S. Afr. J. Sci.*, 101, 29–35.

Bailey, R., A. Gronel, H. Philips, G. Meyers, and E. Tanner (1994), CSIRO Cookbook for quality control of expendable bathythermograph (XBT) data, *Tech. Rep. 220*, CSIRO Mar. Lab., Hobart, Tasmania, Australia.

Belkin, I. M., and A. L. Gordon (1996), Southern Ocean fronts from the Greenwich meridian to Tasmania, *J. Geophys. Res.*, 101, 3675–3696.

Boebel, O., J. Lutjeharms, C. Schmid, W. Zenk, T. Rossby, and C. Barron (2003), The Cape Cauldron: A regime of turbulent inter-ocean exchange, *Deep Sea Res.*, 50, 57–86.

Book, J. (1998), Kuroshio variations off southwest Japan, M.S. thesis, Graduate Sch. of Oceanogr., Univ. of R. I., Kingston, R. I.

Daneshzadeh, Y.-H. C., J. F. Festa, and S. M. Minton (1994), Procedures used at NOAA-AOML to quality control real time XBT data collected in the Atlantic Ocean, *Tech. Rep. ERL AOML-78*, Atl. Oceanogr. and Meteorol. Lab., NOAA, Miami, Fla.

Deacon, G. E. R. (1937), The hydrology of the Southern Ocean, *Discovery Rep.*, 15, 1–124.

de Ruijter, W. P. M., A. Biastoch, S. S. Drijfhout, J. R. E. Lutjeharms, R. P. Matano, T. Pichevin, P. J. van Leeuwen, and W. Weijer (1999), Indian-Atlantic interocean exchange: Dynamics, estimation and impact, *J. Geophys. Res.*, 104, 20,885–20,910.

Ducet, N., P. Y. Le Traon, and G. Reverdin (2000), Global high-resolution mapping of ocean circulation from TOPEX/Poseidon and ERS-1 and -2, *J. Geophys. Res.*, 105, 19,477–19,498.

Duncombe-Rae, C. M. (1991), Agulhas retroflection rings in the South Atlantic ocean: An overview, *S. Afr. J. Mar. Sci.*, 11, 327–344.

Gladyshev, S., M. Arhan, A. Sokov, and S. Speich (2008), A hydrographic section from South Africa to the southern limit of the Antarctic Circumpolar Current at the Greenwich meridian, *Deep Sea Res. Part I*, 55, 1284–1303.

Gordon, A. L. (1985), Indian-Atlantic transfer of thermocline water at the Agulhas Retroflection, *Science*, 227, 1030–1033.

Legeais, J.-F., S. Speich, M. Arhan, I. J. Ansorge, E. Fahrbach, S. Garzoli, and A. Klepikov (2005), The baroclinic transport of the Antarctic Circumpolar Current south of Africa, *Geophys. Res. Lett.*, 32, L24602, doi:10.1029/2005GL023271.

Lemke, P. (1992), WHP cruise summary information: A12, technical report, Alfred Wegener Inst. fuer Polarforsch. und Meeresforsch., Bremerhaven, Germany.

Le Traon, P. Y., and F. Ogor (1998), ERS-1/2 orbit improvement using TOPEX/POSEIDON: The 2 cm challenge, *J. Geophys. Res.*, 103, 8045–8057.

Le Traon, P. Y., P. F. Nadal, and N. Ducet (1998), An improved mapping method of multisatellite altimeter data, *J. Atmos. Oceanic Technol.*, 15, 522–534.

Levitus, S. (1982), Climatological atlas of the World Ocean, *NOAA/ERL GFDL Prof. Pap. 13*, Geophys. Fluid Dyn. Lab., Princeton, N. J.

Lutjeharms, J. R. E. (1985), Location of frontal systems between Africa and Antarctica: Some preliminary results, *Deep Sea Res.*, *32*, 1499–1509.

Lutjeharms, J. R. E. (1988), Meridional heat transport across the subtropical convergence by a warm eddy, *Nature*, *331*, 251–253.

Lutjeharms, J. R. E. (1996), The exchange of water between the South Indian and South Atlantic oceans, in *The South Atlantic: Present and Past Circulation*, edited by G. Wefer et al., pp. 125–162, Springer, Berlin.

Lutjeharms, J. R. E. (2006), *The Agulhas Current*, 329 pp., Springer, Berlin.

Lutjeharms, J. R. E., and W. J. Emery (1983), The detailed thermal structure of the upper ocean layers between Cape Town and Antarctica during the period Jan–Feb 1978, *S. Afr. J. Antarc. Res.*, *13*, 3–14.

Lutjeharms, J. R. E., and A. L. Gordon (1987), Shedding of an Agulhas Ring observed at sea, *Nature*, *325*, 138–140.

Lutjeharms, J. R. E., and H. R. Valentine (1984), Southern Ocean thermal fronts south of Africa, *Deep Sea Res.*, *31*, 1461–1475.

Lutjeharms, J. R. E., and H. R. Valentine (1988), Eddies at the subtropical convergence south of Africa, *J. Phys. Oceanogr.*, *18*, 761–774.

Meinen, C. S., and D. R. Watts (2000), Vertical structure and transport on a transect across the North Atlantic Current near 42°N, *J. Geophys. Res.*, *105*(21), 21,869–21,891.

Moore, J. K., M. R. Abbot, and J. G. Richman (1999), Location and dynamics of the Antarctic Polar Front from satellite sea surface temperature data, *J. Geophys. Res.*, *104*(C2), 3059–3073.

Nowlin, W. D., and M. Clifford (1982), The kinematic and thermohaline zonation of the Antarctic Circumpolar Current at Drake Passage, *J. Mar. Res.*, *40*, 481–507.

Orsi, A. H., W. D. Nowlin, and T. Whitworth (1993), On the circulation and stratification of the Weddell Gyre, *Deep Sea Res.*, *40*, 169–203.

Orsi, A. H., T. Whitworth, and W. D. Nowlin (1995), On the meridional extent and fronts of the Antarctic Circumpolar Current, *Deep Sea Res.*, *42*, 641–673.

Read, J. F., and R. T. Pollard (1993), Structure and transport of the Antarctic Circumpolar Current and Agulhas Return Current at 40°E, *J. Geophys. Res.*, *98*, 12,281–12,295.

Rintoul, S. R., J. R. Donguy, and D. H. Roemmich (1997), Seasonal evolution of upper ocean thermal structure between Tasmania and Antarctica, *Deep Sea Res. Part I*, *44*, 1185–1202.

Rintoul, S. R., S. Sokolov, and J. Church (2002), A 6 year record of baroclinic transport variability of the Antarctic Circumpolar Current at 140°E from expendible bathythermograph and altimetry measurements, *J. Geophys. Res.*, *107*(C10), 3155, doi:10.1029/2001JC000787.

Rio, M. H., and F. Hernandez (2004), A mean dynamic topography computed over the World Ocean from altimetry, in situ measurements, and a geoid model, *J. Geophys. Res.*, *109*, C12032, doi:10.1029/2003JC002226.

Roether, W., M. Samthein, T. J. Muller, W. Nellen, and D. Sahrhage (1990), Sudatlantik-zircumpolarstrom, reise nr. 11, 3 Oktober 1989–11 Marz 1990, meteor-ber. 90-2, technical report, Univ. of Hamburg, Hamburg, Germany.

Schouten, M. V., W. P. M. de Ruijter, P. J. van Leeuwen, and J. R. E. Lutjeharms (2000), Translation, decay and splitting of Agulhas rings in the south-eastern Atlantic Ocean, *J. Geophys. Res.*, *105*, 21,913–21,925.

Scripps Institution of Oceanography (1985), Cruise report: AJAX, technical report, Texas A&M Univ., College Station, Texas.

Sokolov, S., and S. R. Rintoul (2002), Structure of Southern Ocean fronts at 140°E, *J. Mar. Syst.*, *37*, 151–184.

Sokolov, S., and S. R. Rintoul (2007a), Multiple jets of the Antarctic Circumpolar Current south of Australia, *J. Phys. Oceanogr.*, *37*, 1394–1412.

Sokolov, S., and S. R. Rintoul (2007b), On the relationship between fronts of the Antarctic Circumpolar Current and surface chlorophyll concentrations in the Southern Ocean, *J. Geophys. Res.*, *112*, C07030, doi:10.1029/2006JC004072.

Sokolov, S., and S. R. Rintoul (2009a), The circumpolar structure and distribution of the Antarctic Circumpolar Current fronts: 1. Mean circumpolar paths, *J. Geophys. Res.*, *114*, C11018, doi:10.1029/2008JC005108.

Sokolov, S., and S. R. Rintoul (2009b), The circumpolar structure and distribution of the Antarctic Circumpolar Current fronts: 2. Variability and relationship to sea surface height, *J. Geophys. Res.*, *114*, C11019, doi:10.1029/2008JC005248.

Sokolov, S., B. A. King, S. R. Rintoul, and R. L. Rojas (2004), Upper ocean temperature and the baroclinic transport stream function relationship in Drake Passage, *J. Geophys. Res.*, *109*, C05001, doi:10.1029/2003JC002010.

Speich, S., and M. Arhan (2007), GOODHOPE/Southern Ocean: A study and monitoring of the Indo-Atlantic connections, *Mercator Newslett.*, *27*, 29–41.

Speich, S., and F. Dehairs (2008), MD166 international polar year BONUS-GoodHope cruise report, technical report, Inst. Fr. de Rech. pour l'Exploit. de la Mer, Brest France.

Sun, C., and D. R. Watts (2001), A circumpolar gravest empirical mode for the Southern Ocean hydrography, *J. Geophys. Res.*, *106*, 2833–2855.

Sun, C., and D. R. Watts (2002), Heat flux carried by the Antarctic Circumpolar mean flow, *J. Geophys. Res.*, *107*(C9), 3119, doi:10.1029/2001JC001187.

Swart, S., and S. Speich (2010), An altimetry-based gravest empirical mode south of Africa: 2. Dynamic nature of the Antarctic Circumpolar Current fronts, *J. Geophys. Res.*, doi:10.1029/2009JC005300, in press.

Swart, S., S. Speich, I. J. Ansorge, G. J. Goni, S. Gladyshev, and J. R. E. Lutjeharms (2008), Transport and variability of the Antarctic Circumpolar Current south of Africa, *J. Geophys. Res.*, *113*, C09014, doi:10.1029/2007JC004233.

Watts, R. D., C. Sun, and S. R. Rintoul (2001), A two-dimensional gravest empirical mode determined from hydrographic observations in the Subantarctic Front, *J. Phys. Oceanogr.*, *31*, 2186–2209.

Whitworth, T., and W. D. Nowlin (1987), Water masses and currents of the Southern Ocean at the Greenwich Meridian, *J. Geophys. Res.*, *92*, 6462–6476.

World Ocean Circulation Experiment (2002), World Ocean Circulation Experiment, Global data, version 3.0, technical report, Natl. Oceanogr. Data Cent., Silver Spring, Md.

_____

I. J. Ansorge, J. R. E. Lutjeharms, and S. Swart, Department of Oceanography, University of Cape Town, Private Bag, Rondebosch 7701, South Africa. (sebastiaan.swart@uct.ac.za)

S. Speich, Laboratoire de Physique des Océans, UMR 6523, Université de Bretagne Occidentale, CNRS, IFREMER, 6 Ave. Le Gorgeu, F-29238 Brest, France.